# Microscopic multicluster description of the neutron-rich helium isotopes

K. Varga

*Institute of Nuclear Research of the Hungarian Academy of Sciences,
Debrecen, P. O. Box 51, H-4001, Hungary*

Y. Suzuki and Y. Ohbayasi

*Physics Department, Niigata University, Niigata 950-21, Japan*

The neutron halo structure of $^6$He and of $^8$He is studied in a microscopic three-body and five-body model, respectively. Various cluster arrangements are included to embody a variety of correlations between the clusters. The intercluster wave function is determined with the stochastic variational method. The $^6$He and $^8$He energies are reproduced with the same effective force very well. The radii and densities are compared with the results of empirical analyses. The calculated difference of the neutron and proton radii exceeds 0.8 fm, confirming the thick neutron skin. The two-neutron removal spectroscopic amplitudes are calculated and used for evaluating the momentum distribution and the $\beta$ decay spectrum, which are sensitive to the halo structure. A fair agreement with experiment is obtained.

PACS number(s): 21.60.Gx, 27.20.+n, 23.40.Hc

## I. INTRODUCTION

The measurement of the interaction cross section [1] and the momentum distribution of fragments in neutron removal reactions [2] of the light unstable neutron-rich nuclei revealed the unusually large matter radii, and led to the concept of the so-called halo [3] or neutron skin [4] structure of such nuclei. The description of the halo nuclei has since become a challenge for theoretical nuclear model calculations.

In a previous paper [5], we studied the ground states of the nuclei $^6$He and $^8$He. The $^8$He nucleus, with its extremely large neutron excess, is one of the most intriguing examples of the halo nuclei. To give a realistic description of this nucleus, one has to go beyond the $^6$He+$n$+$n$-type or $^4$He+$(2n)$+$(2n)$-type three-body models, because in the former the assumption of the $^6$He inert core is obviously questionable, while in the latter the assumption of the dineutron clusters may exaggerate the neutron correlation. In fact, it has recently been shown [6] that a picture for $^8$He consisting of $^6$He plus a two-neutron halo is not justified by the fragmentation cross section data of the helium isotopes.

In our microscopic multicluster approach the helium isotopes comprise an $\alpha$ cluster and single-neutron "clusters." In this model, the intercluster wave function is a superposition of terms of different relative coordinate arrangements, and each term is a product of nodeless harmonic oscillator functions with different width parameters. The flexibility of the model enables us to include various kinds of important correlations in the halo nuclei on an equal footing. To determine the combination coefficients, the "stochastic variational method" was used, which is an extraordinarily good procedure to select the

important states.

The present model has some advantages over the previous approaches. Unlike the cluster-orbital shell model [7] and the three-body [8,9] approaches, we do not have to use the passive-core-plus-outer-nucleons approximation and we take into account the Pauli principle properly. Although the halo nuclei have been investigated by different versions of the microscopic cluster model [10], our approach is unique as it treats more than three clusters microscopically.

The aim of this paper is to demonstrate that this model provides realistic wave function of halo nuclei, that is, to show that the physical properties extracted from the wave functions are close to the experimental results.

The plan of this paper is as follows. In Sec. II we briefly sketch the model used. In Sec. III we present the results of the numerical calculations. Section IV contains a summary and some conclusions.

## II. THE MICROSCOPIC MULTICLUSTER MODEL

In this section we briefly outline the most important part of our formalism. A more detailed description is given in our previous paper. To describe the system of $\alpha$ plus $n$ single neutron clusters, we build up a trial function which is a sum over various cluster arrangements $\mu$, each associated with a particular set of intercluster Jacobi coordinates $\rho_1^\mu, \ldots, \rho_n^\mu$. The spins of the clusters are coupled to $S$, and the orbital angular momenta $l_i \equiv l_i^\mu$ belonging to the Jacobi coordinates $\rho_i^\mu$ are coupled to $L$. The wave function of the intercluster motion is approximated by a linear combination of nodeless harmonic oscillator functions of different size parameters:

$$\Gamma^{\mu}_{ikl_i m_i}(\rho^{\mu}_i) = \left[\frac{2^{2l_i+7/2}(\nu^{\mu}_{ik})^{l_i+3/2}}{\sqrt{\pi}(2l_i+1)!!}\right]^{1/2} (\rho^{\mu}_i)^{l_i} \exp[-\nu^{\mu}_{ik}(\rho^{\mu}_i)^2] Y_{l_i m_i}(\hat{\rho}^{\mu}_i), \tag{1}$$

where $\nu^{\mu}_{ik}$ is the $k$th size parameter of the $i$th relative motion in the cluster arrangement $\mu$.

The wave function belonging to arrangement $\mu$ and angular momenta $[S,(l_1...l_n)L]JM$ can be written as

$$\Psi^{\mu}_{[S,(l_1...l_n)L]JM}$$

$$= \sum_K C^{\mu}_{K,l_1,...,l_n} \mathcal{A} \left\{ \left[\Phi_S \Gamma^{\mu}_{K(l_1...l_n)L}(\rho^{\mu}_1,...,\rho^{\mu}_n)\right]_{JM} \right\}, \tag{2}$$

where $\mathcal{A}$ is the intercluster antisymmetrizer, $\Phi_{SM_S}$ is a vector-coupled product of the intrinsic wave function of the $\alpha$ particle, $\Psi_{^4\mathrm{He}}$, and the $n$ neutron spin-isospin functions $\Phi^i$. The function $\Gamma^{\mu}_{K(l_1...l_n)L}$ is a vector-coupled product of the intercluster relative functions $\Gamma^{\mu}_{ikl_i m_i}(\rho^{\mu}_i)$, where $K$ stands for the set of the indices $\{k_1,...,k_n\}$ of the size parameters. The sequence of angular momentum coupling is chosen so as to follow the pattern of the Jacobi coordinates. The intrinsic wave function, $\Psi_{^4\mathrm{He}}$, is constructed from a harmonic oscillator Slater determinant with size parameter $\nu$.

The variational trial function $\Psi_{^6\mathrm{He}}$ ($\Psi_{^8\mathrm{He}}$) of $^6\mathrm{He}$ ($^8\mathrm{He}$) is a combination of different arrangements and the intercluster angular momenta:

$$\Psi = \sum_{\mu} \sum_{l_1...l_n} \Psi^{\mu}_{[S,(l_1...l_n)L]JM}. \tag{3}$$

This function contains a great number of terms, due not only to the different arrangements and angular momenta but, especially, to the various size parameters. Owing to this fact our trial function becomes so flexible that it can describe both various types of correlation between the clusters and the spatially extended halo structure. In the previous paper we tested various methods to select $\nu^{\mu}_{ik}$ that span most adequately the state space, while the dimension of the basis is kept feasible. The most efficient procedure found is the following. We generate size parameter sets randomly chosen from an interval which corresponds to the physically important region. The parameter sets that satisfy an admittance condition are selected to be basis states. We admitted a candidate if it, together with the previously selected basis states, lowers the energy more than a preset value, $\epsilon$=0.005 MeV.

To avoid declaring convergence prematurely during this procedure, after ten failed attempts, we removed the condition, and accepted the next candidate. The repetition of this procedure yields excellent numerical convergence in energy and reduces the number of trial terms considerably.

In this paper we use the same potential as in the previous one, i.e., the central effective interaction of Thompson, LeMere, and Tang [11], restrict ourselves to $L=0, S=0$ and neglect the Coulomb force. This interaction is chosen so as to reproduce the most important low-energy nucleon-nucleon scattering data and therefore it does not bind the dineutron. The parameter $u$ of the interaction was set to reproduce qualitatively the $p_{3/2}$ $\alpha$-nucleon phase shifts and the binding energy of $^6\mathrm{He}$ ($u=1.15$). The nucleus $^7\mathrm{He}$ does not exist in nature, and this interaction does not produce it in a bound state.

In our previous study the size parameter of the $\alpha$ particle was chosen so as to minimize the energy of the $\alpha$ particle ($\nu=0.303$ fm$^{-2}$). This choice, however, gives smaller radii than the empirical values by about 8% for the $\alpha$ particle and for $^8\mathrm{He}$. In the present work we adjusted the radius of the $\alpha$ particle to its realistic value ($\nu=0.270$ fm$^{-2}$), allowing the $\alpha$ particle to be slightly less bound and expecting the radius of $^8\mathrm{He}$ to come closer to the experimental findings (the experimental data and our results are compared in Table I). After fixing the parameter $u$ and $\nu$ the model does not contain any free parameter for the description of $^8\mathrm{He}$.

## III. RESULTS

In the calculation for $^6\mathrm{He}$ we used the same configurations as in the previous work, that is, $l_1=l_2=0$ partial waves for the $\alpha+(nn)$ configuration ($T_{00}$) (the $T_{11}$ channel is Pauli forbidden) and $l_1=l_2=0,1$ partial waves for $(\alpha n)n$ ($Y_{00},Y_{11}$). To elucidate the role of the inclusion of the different cluster arrangements, we repeated our calculation using only the $Y$-type channels but including ($Y_{22}$) and ($Y_{33}$) as well. The energy falls as $-0.382$ MeV (in $\{Y_{00}\}$), $-0.601$ MeV (in $\{Y_{00},Y_{11}\}$), $-0.823$ MeV (in $\{Y_{00},Y_{11},Y_{22}\}$), and $-0.923$ MeV (in $\{Y_{00},Y_{11},Y_{22},Y_{33}\}$). At the same time, the energy in the $\{T_{00},Y_{00},Y_{11}\}$ model space is $-0.990$ MeV, and inclu-

TABLE I. Ground-state energies (in MeV), root mean square matter, proton and neutron radii (in fm) of $^4\mathrm{He}$, $^6\mathrm{He}$, and $^8\mathrm{He}$. Empirical values of the radii are taken from Ref. [4]. Values in parenthesis are from Ref. [15].

|  | $E_{\mathrm{exp}}$ | $E_{\mathrm{theor}}$ | $r^{\mathrm{matter}}_{\mathrm{emp}}$ | $r^{\mathrm{matter}}_{\mathrm{theor}}$ | $r^{\mathrm{neutron}}_{\mathrm{emp}}$ | $r^{\mathrm{neutron}}_{\mathrm{theor}}$ | $r^{\mathrm{proton}}_{\mathrm{emp}}$ | $r^{\mathrm{proton}}_{\mathrm{theor}}$ |
|---|---|---|---|---|---|---|---|---|
| $^4\mathrm{He}$ | $-28.30$ | $-25.243$ | 1.63 (1.57) | 1.63 | 1.64 (1.57) | 1.63 | 1.64 (1.57) | 1.63 |
| $^6\mathrm{He}$ | $-0.975$ | $-0.994$ | 2.33 (2.48) | 2.46 | 2.59 (2.61) | 2.67 | 1.72 (2.21) | 1.80 |
| $^8\mathrm{He}$ | $-3.112$ | $-3.301$ | 2.49 (2.52) | 2.40 | 2.69 (2.64) | 2.53 | 1.76 (2.15) | 1.71 |

sion of higher partial waves ($\{T_{00}, T_{22}, Y_{00}, Y_{11}, Y_{22}, Y_{33}\}$) changes it by less than 5 keV ($-0.994$ MeV). We can conclude, in accordance with Ref. [12], that with the inclusion of different rearrangement terms the higher partial waves may safely be omitted.

For the description of $^8$He we selected the arrangements found dominant previously, but complemented them by some $l = 1$ partial waves as well. Thus the following six channels were coupled:

$$\{[(\alpha n)n]n\}n, [(\alpha n)n](nn), [\alpha(nn)](nn),$$

$$\{[\alpha(nn)]n\}n, \{[(\alpha n)_1 n]_1 n\}n, [(\alpha n)_1 n]_1(nn).$$

The lower indices indicate that $l = 1$ partial waves were taken in the corresponding relative motion. These partial-wave pairs were then coupled to total angular momentum $L = 0$. These configurations of $^8$He, in fact, contain the most important configurations of $^6$He. Using the procedure described above the energy minimum has been reached after 124, 91, 57, 64, 31, 19 steps in the successive channels, lowering the energy, in turn, as $-2.49, -3.07, -3.23, -3.28, -3.29, -3.30$ MeV. By consulting Table I, we see that $^8$He is overbound by about 200 keV. This little overbinding is partly due to the fact that the interaction chosen overbinds $^6$He by 20 keV. If it were fine tuned to reproduce the energy of the $^6$He, a more perfect agreement would be obtained, as discussed in Ref. [5].

We have calculated the rms point matter radii of $^6$He and $^8$He. The results are shown in Table I. Effort was made to extract the radii of these nuclei by using the relevant interaction cross section data. However, the extracted values disagree, as listed in Table I, according to the type of model analysis performed. (See Ref. [13] for a detailed theory of evaluating the various fragmentation cross sections for the halo nuclei in the framework of the Glauber theory [14].) The empirical estimates for the difference of the proton and neutron rms radii (thickness of the neutron skin) are 0.87 fm for $^6$He and 0.93 fm for $^8$He (by Ref. [4]) and 0.4 fm for $^6$He and 0.49 fm for $^8$He (by Ref. [15]). The calculated differences of the proton and neutron radii (0.87 fm for $^6$He and 0.82 fm for $^8$He) are close to the recent results of Ref. [4], showing the thick neutron skin. The only striking discrepancy between the empirical estimates and our model is that our calculation gives smaller matter radius for $^8$He than for $^6$He. We shall discuss this point in Sec. IV. To illustrate that the model space has been adequately spanned, we note here that the radius of $^8$He, after about first 150 steps, did not change significantly.

The point nucleon density distribution has also been determined. Although there is no experimental density distribution available, we can compare our results to the qualitative empirical estimates. In a recent paper [4] Tanihata et al. have attempted to deduce the point nucleon density distributions of $^6$He and $^8$He. They assumed a harmonic oscillator density distribution combining the 0s and the 0p orbitals with different harmonic oscillator size parameters. They calculated the interac-

tion cross sections of these nuclei using the optical limit of the Glauber model. The oscillator size parameters were determined by fitting the results to the experiments. However, referring to Ref. [13], we note that the optical limit approximation is not very accurate in evaluating the cross sections of the halo nuclei characterized by spatially extended density distributions. We present our density distributions and their results in Figs. 1(a) and 1(b). The calculated density distributions are not far from the empirical ones and reproduce the most pronounced property, namely the distribution of neutrons extending far beyond that of protons.

Another important quantity that helps to reveal information about the wave function of the halo nuclei is the two-neutron removal spectroscopic amplitude of $^6$He and $^8$He defined by (see e.g., [16])

$$g_{^6{\rm He}}(\mathbf{r}, \mathbf{R}) = \left(\frac{6!}{4!1!1!}\right)^{1/2} \langle \Psi_{^4{\rm He}} \delta(\boldsymbol{\rho}_1 - \mathbf{r})\delta(\boldsymbol{\rho}_2 - \mathbf{R})|\Psi_{^6{\rm He}}\rangle$$

(4)

and

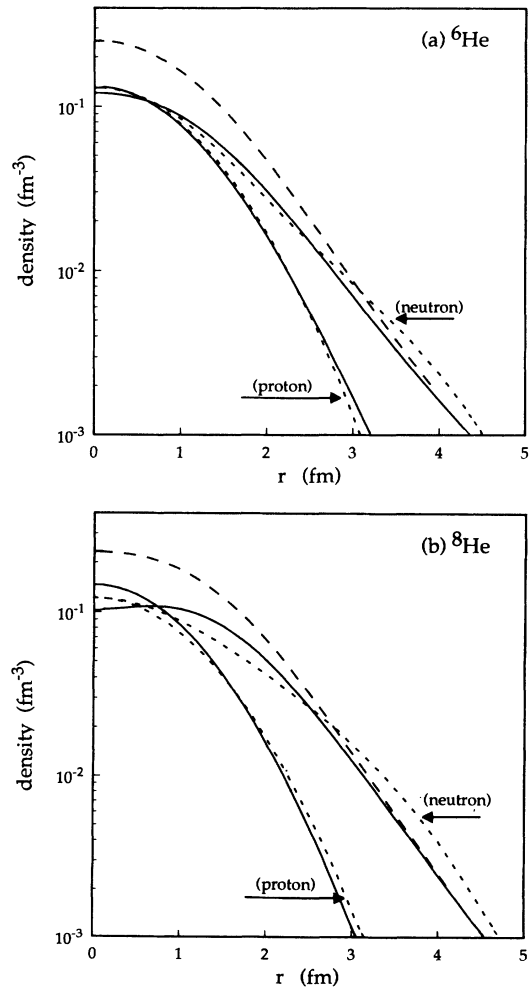

FIG. 1. Empirical (short-dashed line) and theoretical (solid line) proton and neutron density of $^6$He (a) and $^8$He (b). The long-dashed line shows the calculated matter density. The distributions are normalized to the number of nucleons.

$$g_{\text{8He}}(\mathbf{r}, \mathbf{R}) = \left(\frac{8!}{6!1!1!}\right)^{1/2} \langle \Psi_{\text{6He}} \delta(\boldsymbol{\rho}_1 - \mathbf{r})\delta(\boldsymbol{\rho}_2 - \mathbf{R})|\Psi_{\text{8He}}\rangle.$$

$$(5)$$

Here $\boldsymbol{\rho}_1$ is a Jacobi coordinate connecting two neutrons and $\boldsymbol{\rho}_2$ is the Jacobi coordinate connecting the c.m. of these two neutrons with the c.m. of the rest; $\mathbf{r}$ and $\mathbf{R}$ are respective parameter coordinates. Note that the intrinsic wave function of $^6$He, $\Psi_{\text{6He}}$, in Eqs. (4) and (5) is the same. The norm squares of these amplitudes (the two-neutron removal spectroscopic factors) are $\langle g_{\text{6He}}|g_{\text{6He}}\rangle = 1.39$ and $\langle g_{\text{8He}}|g_{\text{8He}}\rangle = 1.36$. These spectroscopic factors are larger than unity but this is not surprising as the two-neutron spectroscopic factors in the pure harmonic oscillator limit, i.e., when the wave function of the relative motions are shell model harmonic oscillator functions of the same size parameters, are $\frac{13}{8}$ and $\frac{13 \times 25}{8 \times 24}$ for $^6$He and $^8$He, respectively [16].

The radial spectroscopic amplitudes

$$g^0_{\text{6He}}(r, R) = \int d\hat{\mathbf{r}} Y_{00}(\hat{\mathbf{r}})^* \int d\hat{\mathbf{R}} Y_{00}(\hat{\mathbf{R}})^* g_{\text{6He}}(\mathbf{r}, \mathbf{R}) \quad (6)$$

and

$$g^0_{\text{8He}}(r, R) = \int d\hat{\mathbf{r}} Y_{00}(\hat{\mathbf{r}})^* \int d\hat{\mathbf{R}} Y_{00}(\hat{\mathbf{R}})^* g_{\text{8He}}(\mathbf{r}, \mathbf{R}) \quad (7)$$

are plotted in Figs. 2(a) and 2(b), respectively. We note here that the norms of these amplitudes are $\langle g^0_{\text{6He}}|g^0_{\text{6He}}\rangle = 1.31$ and $\langle g^0_{\text{8He}}|g^0_{\text{8He}}\rangle = 1.32$, thus about 95% of the spectroscopic amplitudes lie in the subspace of the $l_1 = 0, l_2 = 0$ partial waves. Our model gives qualitatively the same spectroscopic amplitudes for $^6$He as the three-body models [9,10], that is, it shows two prominent peaks: the "dineutron" peak ($r = 1$ fm, $R = 4$ fm) where the two neutrons are close to each other, and the "cigarlike" configuration, with two neutrons at almost the opposite sides of the $\alpha$ particle ($r = 2.75$ fm, $R = 2$ fm). The two-neutron removal spectroscopic amplitude of $^8$He has a shape rather similar to that of $^6$He, although it is spatially more compact. The positions of its peaks are almost the same as in the case of $^6$He, the magnitudes of the peak are, however, about 1.25 times higher than those of $^6$He.

The two-neutron spectroscopic amplitude defined above can be tested by experimental data such as the momentum distribution of the fragment in the two-neutron removal reactions and the $\beta$-decay spectrum.

The normalized momentum distribution of the fragment in one direction is given by

$$\rho(k_x) = \frac{1}{\langle g|g\rangle} \int \int dk_y dk_z d\mathbf{q}|\hat{g}(\mathbf{q}, \mathbf{k})|^2, \quad (8)$$

where $\hat{g}(\mathbf{q}, \mathbf{k})$ is defined as

$$\hat{g}(\mathbf{q}, \mathbf{k}) = \int \int \frac{d\mathbf{r} d\mathbf{R}}{(2\pi)^3} e^{-i\mathbf{q}\mathbf{r} - i\mathbf{k}\cdot\mathbf{R}} g(\mathbf{r}, \mathbf{R}). \quad (9)$$

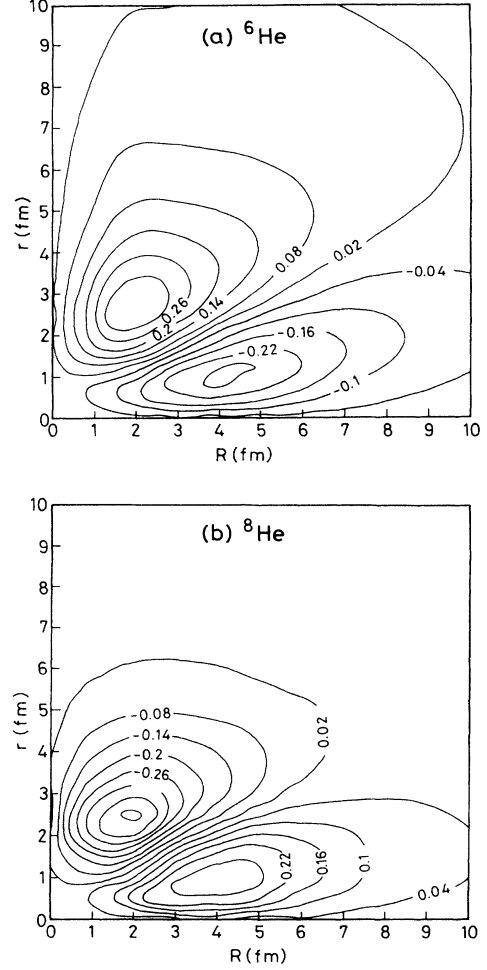In this equation we assumed that the momentum distribution measured in fragmentation reactions is propor-



FIG. 2. Two-neutron removal spectroscopic amplitudes: $rRg^0_{\text{6He}}(r, R)$ and $rRg^0_{\text{8He}}(r, R)$. The value of the magnitude (in fm) as a function of $r$ and $R$ is written on the contour lines.

tional to the momentum distribution $|\hat{g}(\mathbf{q}, \mathbf{k})|^2$ of the fragment and the neutrons in the projectile. In general, the reaction dynamics of the two-neutron removal process gives modifications to Eq. (8). The change for the longitudinal momentum distribution was found to be small at high energies [17]. The transverse momentum distribution at high energies has not so far been analyzed fully with the reaction dynamics included, but the shape of the transverse and the longitudinal momentum distribution in the region of low momentum transfer was found to be quite similar [18]. Therefore we may assume that the observed transverse distribution can be safely compared to the momentum distribution calculated with the spectroscopic amplitude. The experimental and calculated momentum distributions of the $^4$He fragment in the two-neutron removal reaction ($^6$He,$^4$He) [2] and of the $^6$He fragment in ($^8$He,$^6$He) [19] are compared in Figs. 3(a) and 3(b). The characteristic features of the momentum distributions are well reproduced particularly in the case of $^6$He [Fig. 3(a)]. The width of the momentum distribution of $^8$He is slightly wider than in the experiment [Fig.
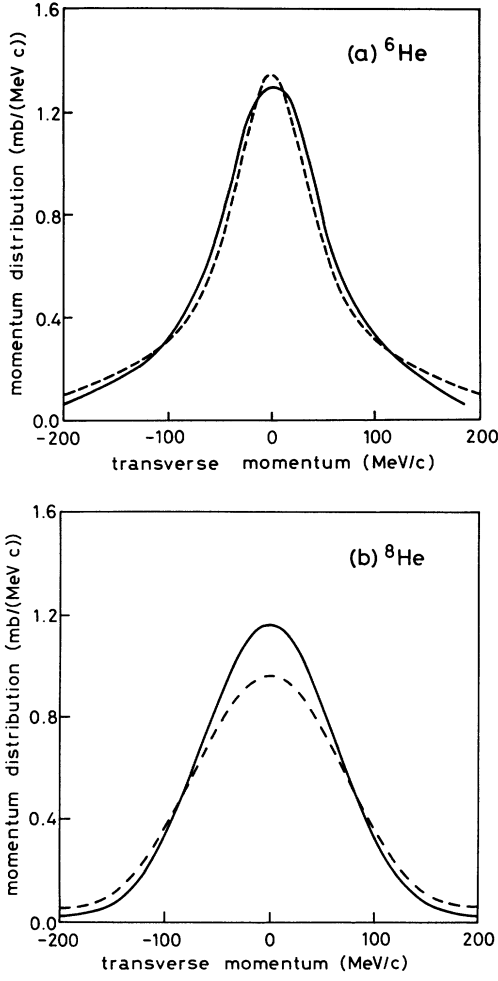
FIG. 3. Experimental (solid line) and theoretical (dashed line) normalized transverse momentum distribution of the $^4$He fragment in the ($^6$He,$^4$He) [2] and the $^6$He fragment in the ($^8$He,$^6$He) [19] two-neutron removal reaction on a carbon target. The two-neutron removal reaction cross sections are $189 \pm 14$ mb and $202 \pm 17$ mb for $^6$He and $^8$He, respectively.



FIG. 4. Absolute value of $R \int dr r^2 F_d(r) g^0_{^6\mathrm{He}}(r, R)$ as a function of $R$.

ity between the $\alpha$ particle and the deuteron, and $G_\beta = 2.996 \times 10^{-12}$ is the dimensionless $\beta$-decay constant. The phase space factor, or Fermi integral, $f$ depends on the kinetic energy $Q - E$ available for the electron and the antineutrino. The mass difference between the initial and final particles is 2.03 MeV. The Gamow-Teller (GT) reduced transition probability is to a fair approximation

$$B_{\mathrm{GT}}(E) = 6\lambda^2 \langle F_d(r)\chi_E(R)|g^0_{^6\mathrm{He}}(r, R)\rangle^2, \qquad (11)$$

where $F_d(r)$ is the radial part of the deuteron wave function and $\chi_E$ is the $\alpha$-deuteron relative wave function in the final state. See Ref. [10] for details. Figure 4 displays the effective function, $R \int dr r^2 F_d(r) g^0_{^6\mathrm{He}}(r, R)$, as a function of $R$. The asymptotic behavior at large distances is described well enough to calculate the $\beta$-decay spectrum. The calculated probability, $\frac{dW}{dE}$, shown in Fig. 5, reproduces the experiment [21] reasonably well. The quality of agreement is very similar to that of Ref. [20],

3(b)]. This indicates that the relative motion between $^6$He and the two neutrons in the halo should extend spatially a little further. This point may be related to the fact that the calculated $^8$He energy is overbound by about 200 keV.

The two-neutron removal spectroscopic amplitude of $^6$He can also be used to calculate the $\beta$-decay rate into $\alpha$ and deuteron. Recent theoretical analyses [10,20] have revealed an extreme sensitivity to the halo description up to distances as large as 15 fm. We show the $\beta$-decay spectrum obtained with our wave function in order to see how good it is at large distances. The $\beta$ delayed deuteron emission transition probability per time and energy units, $\frac{dW}{dE}$, can be expressed as

$$\frac{dW}{dE} = \frac{mc^2}{\pi^4 v \hbar^2} G_\beta^2 f(Q - E) B_{\mathrm{GT}}(E), \qquad (10)$$

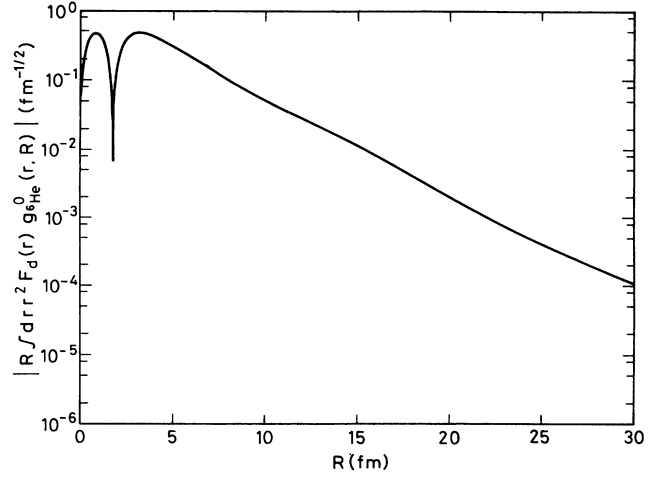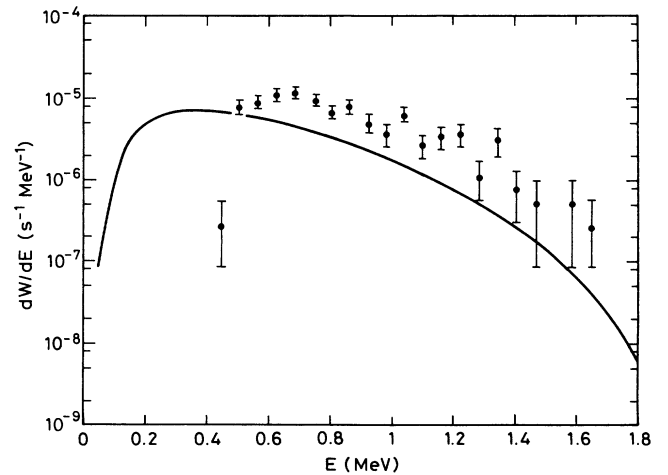where $m$ is the electron mass, $v$ is the relative veloc-



FIG. 5. Transition probability $dW/dE$ per time and energy units (in s$^{-1}$ MeV$^{-1}$) in the c.m. frame as a function of the c.m. energy $E$ (MeV). The experimental points are from Ref. [21].

where a more sophisticated description of the final states is used.

The $\beta$ delayed triton and $\alpha$ spectra of $^8$He have also been measured [21]. In this case the possibility of the direct decay mechanism through the $^5$He resonance, that is, $^8$He $\to$ $t+^5$He$(3/2^-)$ $+$ $e^-+\bar{\nu}_e$ and $^5$He $\to$ $\alpha + n$, is ruled out because a simple symmetry argument predicts vanishing GT matrix elements for the $\beta$ decay. A more careful consideration on the $\beta$-decay mechanism is needed to test the $^8$He wave function with use of the $\beta$-decay spectra of $^8$He.

## IV. SUMMARY

The use of the stochastic variational method allows us to treat the light neutron-rich nuclei as a multicluster system. This method helps to keep the dimension of the variational basis low and ensures that the wave function is good enough to describe the extended neutron halo. In this paper we have calculated the ground-state energy, wave function, and some physical properties of the nuclei $^6$He and $^8$He in a fully microscopic framework. The inclusion of various rearrangement cluster configurations was shown to be quite effective to describe the halo structure of the helium isotopes.

We set the only parameter of our simple central nucleon-nucleon interaction to give the nearly correct ground-state energy of $^6$He and by using this interaction we reproduced the ground-state energy of $^8$He with fair accuracy.

We have calculated the proton, the neutron, and the point matter rms radii of these nuclei. The difference between the neutron and proton radii in our model, i.e., the thickness of the neutron skin, is in perfect agreement with the empirical findings. Unlike empirical estimates, our model gives a little larger rms radius for $^6$He than for $^8$He. This discrepancy may reflect the effect of the overbinding ($\sim$ 200 keV) of $^8$He or the use of a not fully adequate effective interaction (e.g., the neglect of the spin-orbit force) but, at the same time, one may be inclined to accept this result since the binding energy of $^8$He (3.112 MeV) is much larger than the binding energy of $^6$He (0.975 MeV). To estimate the effect of the overbinding of $^8$He on the rms matter radii of $^6$He and $^8$He, we set the parameter $u$ to 1.145. This choice gives 0.87 MeV for the binding energy of $^6$He, and results in less overbinding of $^8$He ($\sim$ 160 keV). While in this calculation the rms matter radius of $^6$He increased ($r = 2.48$ fm), that of $^8$He hardly changed, in fact it decreased by 0.004 fm. Therefore, the overbinding does not seem to be responsible for the result that the rms matter radius of $^6$He is calculated to be larger than that of $^8$He. The calculated result that both the proton and neutron radii of $^6$He are larger than those of $^8$He may be understood if one assumes that the distance between the center of mass of the $\alpha$ particle in $^6$He and the center of mass of $^6$He is larger than the corresponding quantity in the case of $^8$He. To understand the reason of the discrepancy of the radii, one has to use a more sophisticated effective interaction, or the extraction of the proton or neutron radii from the interaction cross section data has to be carefully reinvestigated.

We have determined the proton, the neutron, and the matter distributions. The results are in accord with the empirical estimates and the relativistic mean field calculations [4].

The two-neutron removal spectroscopic amplitudes have been calculated and used to calculate the momentum distributions of the fragments arising from the two-neutron removal reaction and the $\beta$ decay of $^6$He into $\alpha$ and deuteron. The results are in fair agreement with experiment.

[1] I. Tanihata, H. Hamagaki, O. Hashimoto, Y. Shida, N. Yoshikawa, K. Sugimoto, O. Yamakawa, T. Kobayashi, and N. Takahashi, Phys. Rev. Lett. **55**, 2676 (1985).

[2] K. Kobayashi, Nucl. Phys. **A538**, 343c (1992).

[3] P. G. Hansen and B. Jonson, Europhys. Lett. **4**, 409 (1987).

[4] I. Tanihata, D. Hirata, T. Kobayashi, S. Shimoura, K. Sugimoto, and H. Toki, Phys. Lett. B **289**, 261 (1992).

[5] K. Varga, Y. Suzuki, and R. G. Lovas, Nucl. Phys. **A571**, 447 (1994).

[6] Y. Suzuki, T. Kido, Y. Ogawa, K. Yabana, and D. Baye, Nucl. Phys. **A567**, 957 (1994).

[7] Y. Suzuki and K. Ikeda, Phys. Rev. C **38**, 410 (1988); Y. Suzuki and J. J. Wang, *ibid.* **41**, 736 (1990); Y. Suzuki, Nucl. Phys. **A538**, 395 (1991).

[8] V. I. Kukulin, V. M. Krasnopol'sky, V. T. Voronchev, and P. B. Sazonov, Nucl. Phys. **A417**, 128 (1984); **A453**,

365 (1986); A. Ghovanlou and D. R. Lehman, Phys. Rev. C **9**, 1730 (1974).

[9] M. V. Zhukov, B. V. Danilin, D. V. Fedorov, J. M. Bang, I. J. Thompson, and J. S. Vaagen, Phys. Rep. **231**, 150 (1993); M. V. Zhukov, A. A. Korsheninnikov, and M. H. Smedberg, this issue, Phys. Rev. C **50**, R1 (1994).

[10] D. Baye, Y. Suzuki, and P. Descouvmont, Prog. Theor. Phys. **91**, 271 (1994).

[11] D. R. Thompson, M. LeMere, and Y. C. Tang, Nucl. Phys. **A286**, 53 (1977).

[12] M. Kamimura, Phys. Rev. A **38**, 621 (1988).

[13] Y. Ogawa, K. Yabana, and Y. Suzuki, Nucl. Phys. **A543**, 722 (1992).

[14] R. J. Glauber, *Lectures in Theoretical Physics* (Interscience, New York, 1959), Vol. 1, p. 315.

[15] I. Tanihata, T. Kobayashi, O. Yamakawa, S. Shimoura, K. Ekuni, K. Sugimoto, N. Takahashi, T. Shimoda, and

H. Sato, Phys. Lett. B **206**, 592 (1988).

[16] K. Varga and R. G. Lovas, Phys. Rev. C **43**, 1201 (1991).

[17] Y. Ogawa, Y. Suzuki, and K. Yabana, Nucl. Phys. **A** (in press).

[18] T. Fujita and J. Hüfner, Nucl. Phys. **A343**, 493 (1980).

[19] T. Kobayashi, O. Yamakawa, K. Omata, K. Sugimoto, T. Shimoda, N. Takahashi, and I. Tanihata, Phys. Rev. Lett. **60**, 2599 (1988).

[20] A. Csótó and D. Baye, Phys. Rev. C **49**, 818 (1994).

[21] M. J. G. Borge, L. Johannsen, B. Jonson, W. Kurcewicz, T. Nilsson, G. Nyman, K. Riisager, O. Tengblad, and K. Wilhelmsen, Nucl. Phys. **A560**, 664 (1993).